

Morphology, Luminescence, and Optical Properties of Tb- and Li-Codoped ZnO Elongated Nano- and Microstructures

Fernando Pavón, Rocío Ariza, Ana Urbieto, and Paloma Fernández*

A variety of morphologies of ZnO elongated nano- and microstructures doped with Li and Tb are obtained by a vapor–solid method. The amount of Tb incorporated depends on the morphology which is controlled by the amount of Li in the initial mixture and the growth conditions. X-ray diffraction and Raman experiments show the good crystalline quality of the samples. A small quantity of Tb³⁺ ions seems to be present in the structures, as both cathodoluminescence and photoluminescence suggest. The intensity of the ZnO and Tb³⁺ intrashell emission bands is strongly influenced by the amount of Li due to the different positions that it can occupy in the ZnO lattice. This fact leads to variations in the defect structure that change the concentration of native defects and the rare earth surroundings. The elongated structures also show waveguiding behavior and Fabry–Perot optical resonant modes with good quality factor.

Nevertheless, controlling the properties of these structures through doping is a key factor for the developing of these remarkable applications. Many different dopants have been used in the past years for this purpose. In particular, rare earth ions can strongly modify the optical properties and the charge separation between photogenerated electrons and holes, both aspects are crucial in the optoelectronic and photocatalytic behavior.^[9,10] Among them, Tb³⁺ is an ion of interest since its main luminescent transition is located at 544 nm (2.28 eV), which corresponds to one of the primary colors. In a previous work,^[11] nano- and microstructures of ZnO doped with Tb were successfully obtained using vapor–solid deposition as


1. Introduction

ZnO elongated nano- and microstructures have attracted increasing attention in the past decades. The variety of morphologies that can be achieved by changing the growth conditions^[1] and the diversity of dopants that can be used to foster these properties^[2,3] make them good candidates for the next generation of nanodevices. The wide bandgap (3.37 eV at room temperature), high exciton binding energy (around 60 meV) and high refractive index enables their utilization as optoelectronic devices^[4] and nanolasers.^[5] ZnO also shows a high piezoelectric coefficient, leading to the possibility of fabrication of nanoresonators or nanocantilevers.^[1] Moreover, it is a cheap and biocompatible material that can be used as biosensor,^[6] photocatalyst,^[7] or bactericide.^[8]

We showed that the structures morphology can be controlled by the precursors and growth conditions used and that they can be utilized as waveguides and optical resonant cavities. In this regard, codoping with other ion, such as Li, is an interesting possibility since it has been reported that Li improves the optical performance of the structures.^[12,13] In fact, Er and Li codoping of ZnO elongated nanostructures with good optical properties have been already achieved.^[14] In the case of Tb and Li codoping, nanoparticles grown by sol–gel method^[15] or coprecipitation^[16] have been previously investigated. On the other hand, alkali metals have been proposed as suitable dopants to attain p-type conductivity in ZnO by introducing shallow acceptors, however, their efficiency is limited due to the formation of compensating interstitials.^[17] Combining two dopants with different charge can lead to balance mechanisms in the material that can completely change its defect structure and, consequently, influence in both the optical and the electronic properties.^[18]

In this work, Tb–Li codoped ZnO nano- and microstructures have been obtained by a vapor solid method (VS). Although, vapour–liquid–solid method (VLS) is most frequently used, the main advantage of VS is that no catalyst is required, hence possible contamination is avoided. Depending on the lithium initial content, different morphologies are grown, their shape and face regularity and number increases as Li concentration does. XRD and Raman experiments have been performed to structurally characterize the samples which present good crystalline quality. Luminescence investigations show that both Li and Tb are incorporated into the ZnO lattice affecting the defect structure of the material and hence the relative intensity of

F. Pavón, R. Ariza, A. Urbieto, P. Fernández
Departamento de Física de Materiales
Facultad de Ciencias. Físicas
Universidad Complutense de Madrid
Ciudad Universitaria s/n, 28040 Madrid, Spain
E-mail: arana@ucm.es

 The ORCID identification number(s) for the author(s) of this article can be found under <https://doi.org/10.1002/pssa.202100805>.

© 2022 The Authors. physica status solidi (a) applications and materials science published by Wiley-VCH GmbH. This is an open access article under the terms of the Creative Commons Attribution License, which permits use, distribution and reproduction in any medium, provided the original work is properly cited.

DOI: 10.1002/pssa.202100805

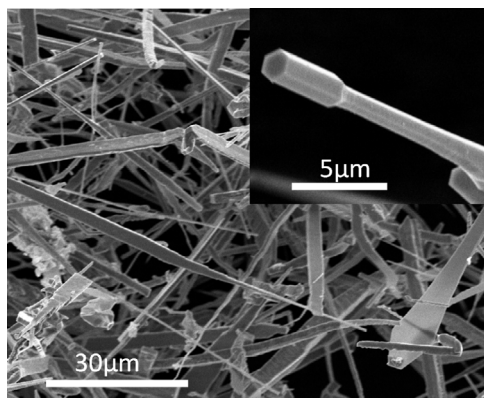


Figure 1. SEM image of the structures obtained onto the quartz tube in samples with 5%wt. Tb_4O_7 and no Li added.

the emission bands in the UV and visible ranges. From the μ -PL images, it is demonstrated that the structures can be used as waveguides and that, in some cases, Fabry–Perot optical cavity modes can be established with good quality factors.

2. Results and Discussion

Nano- and microstructures are grown in all the samples after the thermal treatments. However, the morphology and sizes vary depending on the initial content of Li_2O . The zone temperature of the furnace where the structures are obtained is also influencing their shape and dimensions which is directly related to the growth temperature of the structures, as it has been previously observed.^[19] In addition, larger amounts of structures are obtained in the samples with higher concentration of Li_2O (5 and 10%wt) in the initial mixture.

Figure 1 shows the structures obtained on the reference samples where no Li was added. In this case, the structures are mainly grown on the walls of the quartz tube and consist of thin ribbons of about 200 nm thick, hundreds of μm long and 3–8 μm width. In some cases, wires with hexagonal cross section are also observed (inset).

When a small amount of Li_2O is added to the samples (1%wt), some structures start to grow also on the surface of the alumina

boat. Their morphology changes from ribbons to wires and sword-like plates. The length of these structures rises to several mm and the width varies between hundreds of nm to several μm (**Figure 2a**). Besides, some structures can also be observed on the surface of the pellet (**Figure 2b**). In this case, rods with lengths of 30–50 μm and diameters below 5 μm are obtained. Comparing these results with those obtained previously for ZnO:Tb ,^[11] we infer that the main changes in morphology and growth temperature could be related to the addition of Li into the samples which is further confirmed by the observations in the samples with increasing amount of Li_2O . This could be due to the fact that the melting temperature of the compounds in the precursor mixture is different, hence if the proportion of each component is modified, the melting temperature of the precursor would be also different, and hence the conditions to get the saturation atmosphere required for the deposit to take place.

In the samples with 5 and 10 wt% of Li_2O , a more homogeneous distribution in size and morphology of the structures is obtained, their amount is also increased. Ribbons and sword-like formations of about 5 μm thick which grow both on the boat and on the quartz tube walls are clearly observed (**Figure 3a**). Moreover, their faces are better formed with, generally, a more regular shape. In some areas of the sample with 10 at% of Li_2O , structures formed by a long wire (tens of μm) in which spherical beads (few μm in diameter) are inserted can be observed (**Figure 3b**). This last type of morphology has been previously observed in Li doped ZnO structures obtained by the same method^[19] and consist of a combination of a ZnO wire and Li_2SO_4 balls, indicating that the solubility limit of Li could be already reached in the ZnO structures and the excess of Li is reacting with the evaporated S coming from the pellets.

Compositional analysis of the structures has been performed by EDX in the SEM. Although Li content cannot be obtained by this technique due to its low atomic number, the presence and distribution of Tb in the structures is determined from the spectra recorded on the different morphologies. In the case of the reference sample, the amount of Tb incorporated to the structures does not significantly depend on the morphology and varies between 1 and 3 at%, in agreement with previous results.^[11] However, when Li_2O is added into the initial mixture large differences in the Tb content is observed related to variations in the morphology and size. In the case of the structures which grow on

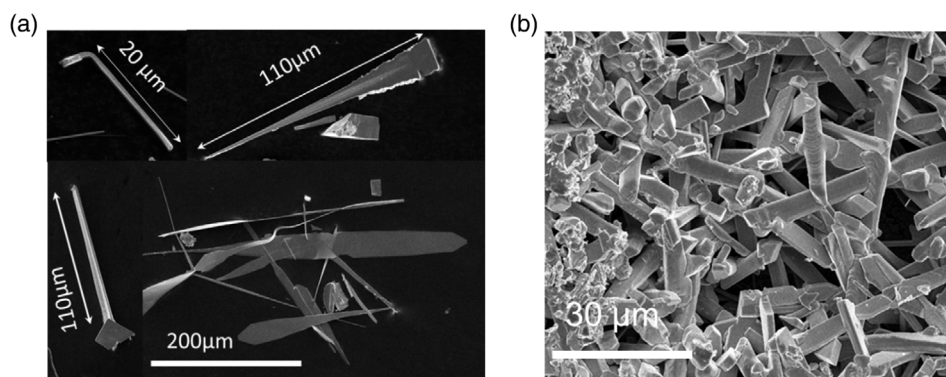


Figure 2. SEM images of the different structures obtained in samples with 5%wt. Tb_4O_7 and 1% wt. Li_2O . a) Structures grown on the alumina boat and b) structures grown on the surface of the pellet.

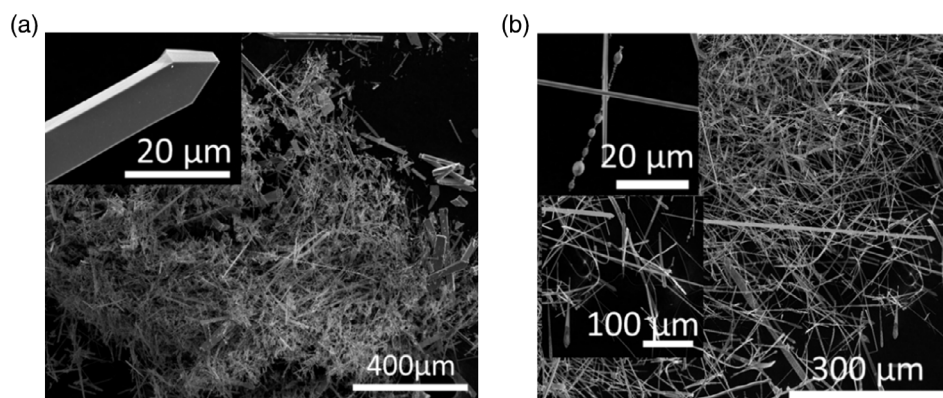


Figure 3. SEM images of the different morphologies obtained on the samples with a) 5%wt. and b) 10% wt. Li_2O content.

the alumina boat in the sample with lower Li_2O content (Figure 2a), sizes and shapes are not homogeneous, and this fact is also reflected in Tb content which varies from 5 to 13 at% depending on the particular structure analyzed. This large variation could be related to the different incorporation of Li which leads to the disparity in morphology. Nevertheless, for the structures which grow on the furnace tube in the same samples, whose shape and size are more regular, a homogeneous Tb content of about 5 at% is measured. A similar behavior is observed in the structures obtained from the samples with 5 and 10 wt. Li_2O . In both cases, the ribbons, swords and wires show Tb concentrations of 3–4 at%. A small amount of S is also detected in all the structures analyzed indicating that residual ZnS could remain in the samples after the thermal treatments.

XRD patterns have been performed in all samples. **Figure 4** shows the pattern obtained on the structures grown in the sample with medium content of Li (5 wt% Li_2O). As it can be observed, all the diffraction peaks can be assigned to wurtzite phase of ZnO (JCPDS 00-036-1451), indicating the good

crystallinity of the structures. No significant shifts in the positions of the maxima are detected neither between the different samples nor comparing to pure ZnO. On one hand, Li^+ ionic radius in six-fold coordination (76 pm) is similar to that of Zn^{2+} (74 pm) so that, no significant lattice distortion and, hence, shifts in the XRD maxima are expected. On the other hand, considering that Tb^{4+} ionic radius is 76 pm and that of Tb^{3+} is 92.3 pm, the XRD patterns suggest that most of Tb ions are incorporating as Tb^{4+} since they can occupy substitutional positions in the ZnO lattice with no significant distortion. The excess of charge introduced could be compensated by the formation of Zn vacancies. Nevertheless, some Tb^{3+} ions could also be incorporated modifying the luminescence emissions as will be discussed later.

To further study the crystalline quality of the grown structures, μ -Raman spectra on individual structures from all the samples were also performed (**Figure 5**). In the case of the spectrum from the samples with no Li added, Raman peaks centered at 98, 205, 329, 375, 412 and 436 cm^{-1} are clearly observed. All these

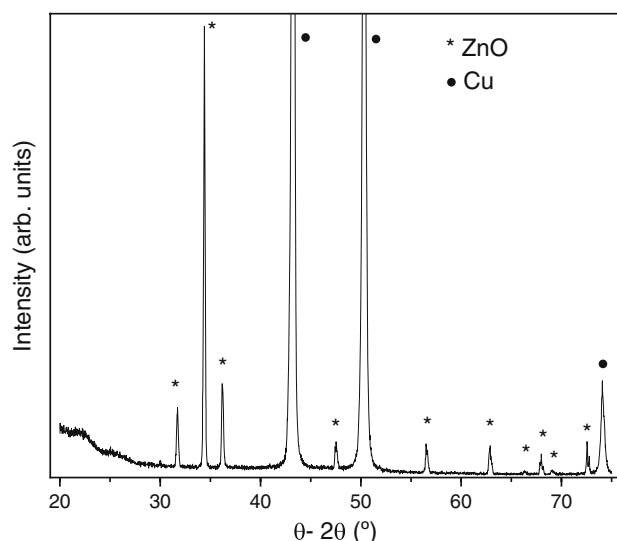


Figure 4. XRD pattern of the structures grown in the sample with 5%wt. of Li_2O . Maxima corresponding to ZnO are marked with *, the reflections marked with • are due to Cu from the sample holder.

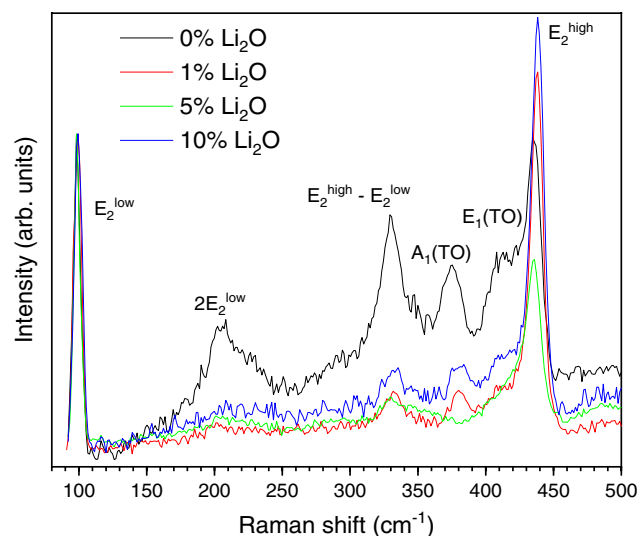


Figure 5. μ -Raman spectra recorded on individual structures obtained on the different samples investigated. All the observed peaks are labeled and can be ascribed to Raman modes of the wurtzite structure of ZnO.

maxima are related to the wurtzite structure of ZnO and its presence indicates the good crystallinity of the structures.^[20,21] No shifts in the positions of the peaks are detected in the spectra from the structures with the different Li contents, showing that its addition does not significantly distort the wurtzite lattice, in agreement with the previous observations in XRD patterns. However, the intensity of some of the peaks decreases which could suggest that the crystalline quality slightly deteriorates. Anyway, the peaks at the 98 and 436 cm⁻¹, which correspond to the main Raman modes in ZnO (E_2^{low} and E_2^{high} , respectively), remain clearly visible revealing that the structures still show good structural quality.

Luminescence properties of the grown structures of the different samples have been investigated by cathodoluminescence in the SEM. The normalized spectra performed at 100 K are shown in **Figure 6a**. Two main bands can be observed, a UV emission centered at 3.3 eV which corresponds to the near

band edge of ZnO which splits in two components in the spectra from samples with higher Li₂O content (blue line), and an intense and broad visible band centered between 2.3 and 2.4 eV which corresponds to the well-known green band of ZnO. The complex nature of the latter can be appreciated in the variations in shape and position observed for the spectra recorded on the different samples. The band is centered at 2.4 eV for the sample with no added Li and shifts to lower energies in the codoped samples. This shift is due to the increase in intensity of the emission components in the low energy side. To better observe the different luminescence components, a single spectrum recorded on the structures grown with 5% wt. Tb₄O₇ and 5% wt. Li₂O is also shown (**Figure 6b**), the components have been marked with arrows and are located at 2.42, 2.31, 2.03, 1.9, and 1.74 eV. The visible luminescence band of ZnO is normally associated to the existence of several native defects such as zinc interstitials^[22] or oxygen vacancies,^[23] however it can also include emissions due to other native defects and impurities, such as Li. Besides, the intrashell $^5D_4 \rightarrow ^7F_x$ electric dipole transitions of Tb³⁺ ions, located at 2.53, 2.27, 2.12, and 2 eV (490, 545, 585, and 620 nm, respectively), can also contribute to this broadband.

The observed differences can be explained considering the inclusion of Li into the ZnO lattice and its influence in the defects structure of the material. It is known that Li does not produce any luminescence band by itself, however, the different positions that can occupy in the ZnO lattice, either as interstitial (Li_i) or substitutional (Li_{zn}) influences the concentration of native defects.^[24,25] At low Li content (red line spectrum in the figure), a shoulder at 2.0 eV is clearly observed, but the intensity of this component decreases as the Li content increases. This band has been related by some authors to differences in the rate of radiative transition from donors to the intrinsic acceptor defects (V_{zn} or O_i).^[26] In our case, at low dopant content, the Li atoms would be located at interstitial positions, at the same time, Tb⁴⁺ ions would replace Zn²⁺ cations of the lattice. Due to the charge imbalance, for each Tb⁴⁺ ion settled, two Zn²⁺ cations must be replaced which leads to an increase of V_{zn} and the rise of the intensity of the low energy components of the emission band. As the Li content grows, the Li atoms start to occupy substitutional positions,^[19] filling the Zn vacancies, so that, the intensity of these components decreases. Additionally, although XRD patterns suggest that most of the Tb ions are incorporated as Tb⁴⁺, a small amount of Tb³⁺ ions can also enter the ZnO lattice. In this case, luminescence emissions corresponding to intrashell 4f transitions could also be responsible of some of the shoulders observed in the CL spectra. The fact that some Tb³⁺ is also incorporating is further supported by the splitting in two bands of the near band edge emission observed. This behavior has been previously observed in ZnO:Tb thin films grown by sputtering^[27] and nanorods and nano- and microstructures obtained by electrodeposition^[28] or the vapor–solid method^[11] and it seems to be due to the change in the Zn–O bond length produced by the incorporation of Tb³⁺ which leads to a blue-shift of free excitons emission line.

The effect of the presence of Tb³⁺ ions in the luminescence properties of the structures is better observed in the photoluminescence spectra. **Figure 7** shows the PL spectra recorded at room temperature on the structures grown with 0, 1, 5 and

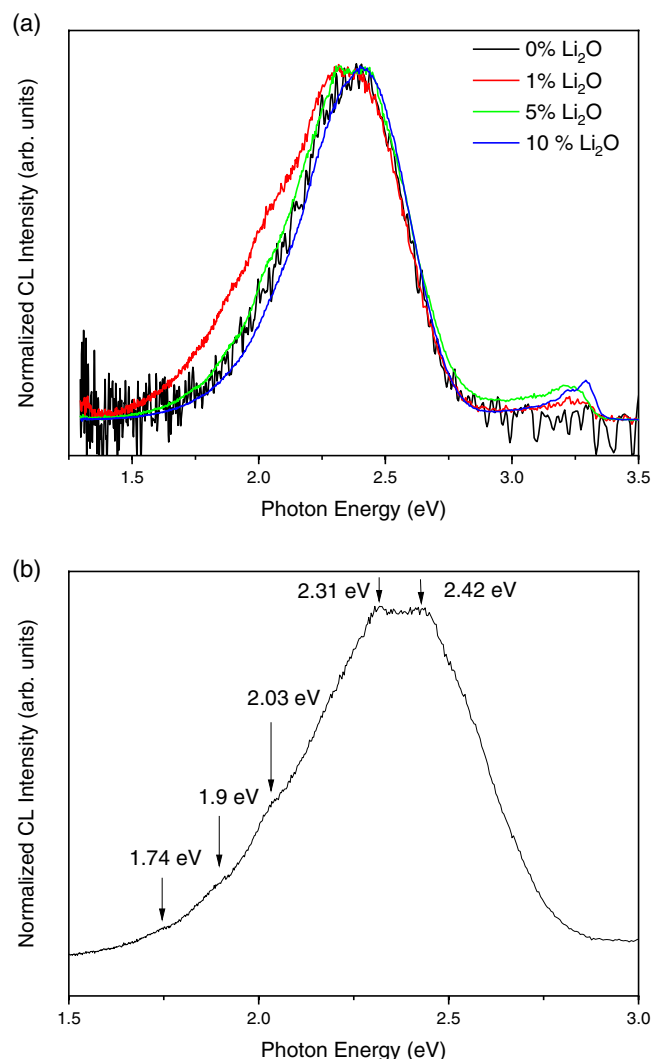


Figure 6. a) Normalized CL spectra at 100 K recorded on the structures grown on the samples with different content of Li₂O. b) Spectrum from the structures obtained in the sample with 5%wt. Tb₄O₇ and 5% Li₂O (green line in part (a)), arrows mark the different emissions that can be resolved.

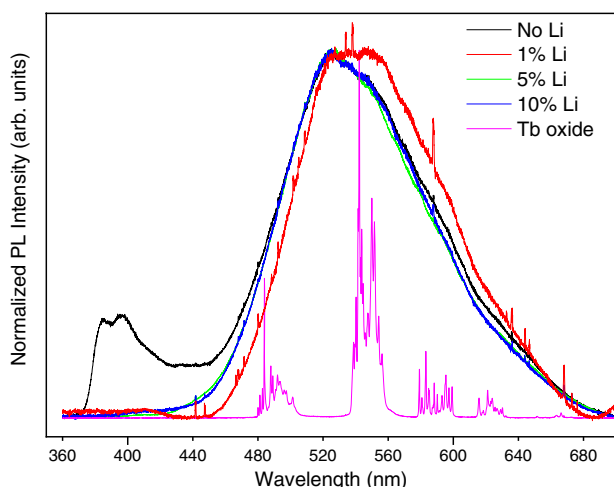


Figure 7. PL spectra of structures grown on the samples with 5 wt% of Tb_4O_7 and 0, 1, 5, and 10 wt% of Li_2O . A spectrum from Tb_4O_7 is also shown for comparison.

10 wt% of Li_2O and 5 wt% of Tb_4O_7 . For comparison, a spectrum from Tb_4O_7 precursor is also shown. As it is observed, the general behavior of the luminescence bands is similar to that studied in the CL experiments. However, in this case, three shoulders at 548 nm (2.26 eV), 590 nm (2.1 eV), and 625 nm (1.98 eV) are detected. Comparing their positions to those of the emission lines coming from the intrashell $^5\text{D}_4 \rightarrow ^7\text{F}_x$ electric dipole transitions of Tb^{3+} ions, it can be suggested that these emissions bands results from the convolution of each the group of lines that form the multiplet. The fact that the lines are not well resolved can be related to the different defect environment which surrounds the Tb ions throughout the structures. As mentioned before, the concentration of Tb into the structures depends on their morphology and the amount of Li incorporated which

affects the defect structure and their concentration, leading to differences in the local crystal structure around the Tb ions.

Finally, the behavior of the Tb–Li codoped structures as waveguides and optical resonant cavities has been also investigated. **Figure 8** shows the μ -PL image of a ribbon structure grown on the sample with 5%wt. Li_2O –5%wt. Tb_4O_7 . As it is observed, the luminescence generated by the excitation laser (point 1) is guided along the structure and exits at its both edges (points 2 and 3). No light losses can be detected throughout the surface of the structure, indicating its good quality as waveguide. Similar results have been reported previously in nano- and microstructures of Tb doped and Er and Li codoped ZnO grown by the same method.^[11,14] To further study this behavior, spectra have been performed for both the luminescence generated at the laser incidence point (point 1) and the light which travels along the structure and exits at one of the edges (point 2), the results are shown in part b of Figure 8. In the spectrum recorded in point 1 (black line), the two emission bands of ZnO related to near band edge emission, peaked at 380 nm, and defects, centered at about 525 nm, are observed. In addition, a set of well resolved peaks superimposed to the green emission band are clearly visible. The presence of these peaks suggests that the ribbon is acting as optical resonant cavity since they are equally spaced.^[13,29,30] The spectrum of the guided light recorded on point 2 (red line) shows two main differences. First, the modulations are no longer visible, indicating that these particular resonant modes cannot propagate along the structure axis, and second, the near band edge emission is shifted to longer wavelengths (400 nm). This can be due to the reabsorption of the luminescence components at higher wavelengths, i.e., the free exciton emission, by the ZnO which is a very likely process that has been observed previously^[11,14]

The optical resonant modes have been also observed in other morphologies obtained. In **Figure 9** the results from a sword-like structure with rectangular cross-section are shown. From the SEM image (part a), a length of 200 μm and a width of

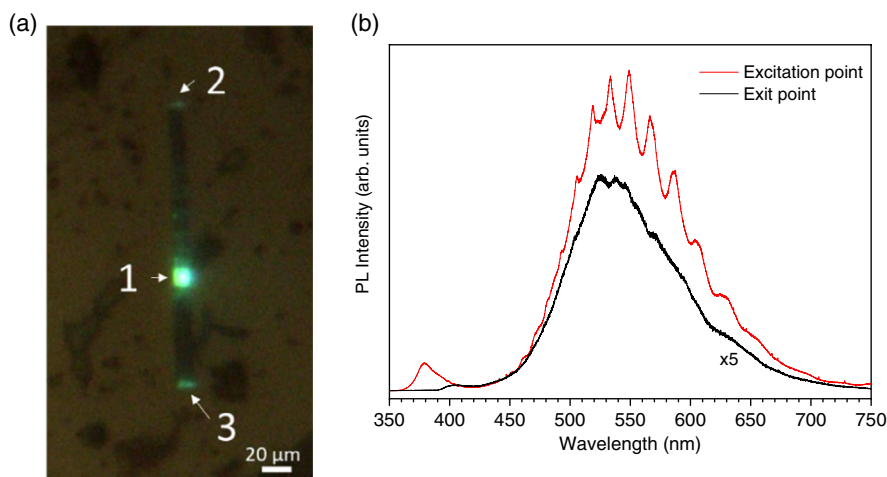


Figure 8. a) μ -PL image of a ribbon grown on the sample with 5% wt. Li_2O –5%wt. Tb_4O_7 . The arrows mark the points of laser incidence (point 1) and light exit at the edges of the structure (points 2 and 3). b) Spectra recorded at excitation point (black line) and exit point (red line) of the structure in part b. Superimposed peaks related to resonant cavity modes are clearly visible in the spectrum from the excitation point. In this particular case, since the peak structure is complex and different modes (transverse and longitudinal) seem to be mixed, the exact configuration of the established modes cannot be elucidated.

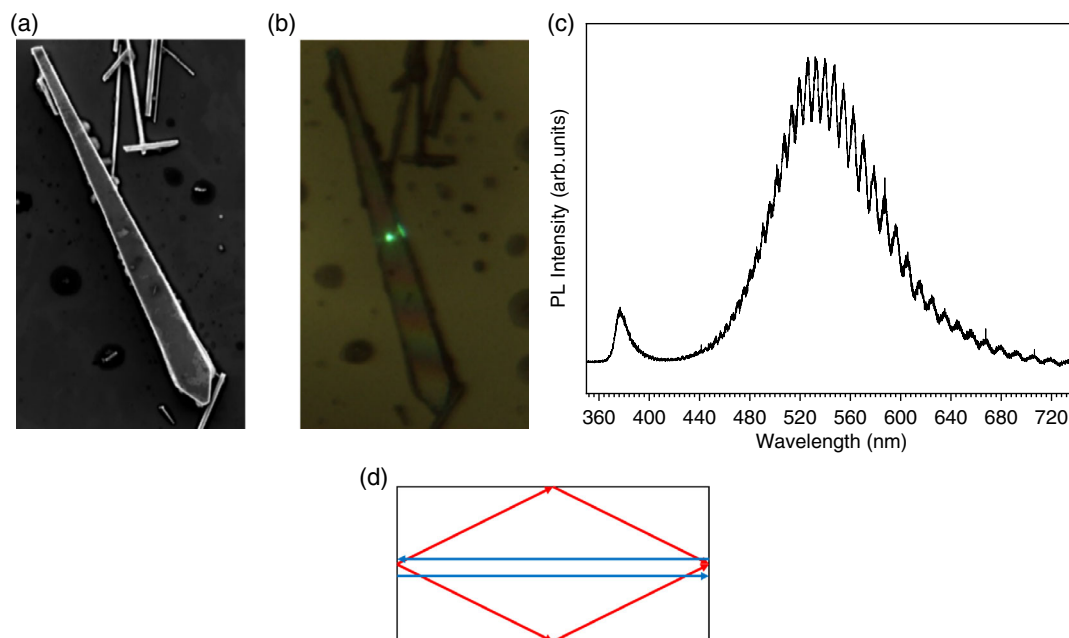


Figure 9. a) SEM and b) μ -PL images of a sword-like structure obtained in the sample with 5% wt. Li₂O–5% wt. Tb₄O₇, c) PL spectrum recorded on the incident point of the excitation laser; d) schematic representation of the possible resonance paths in the sword-like structure, FP modes (blue line) and WG modes (red line).

12.95 μm are measuring for this particular structure. The μ -PL image (part b) shows the point where the luminescence is generated by the excitation laser, the spectrum is shown in part (c) of the figure where the optical resonant modes are clearly visible. Optical resonant modes are originated by the internal reflection of confined light inside the structures. Due to the high refractive index that ZnO ($n_{\text{ZnO}} \approx 2$) has with respect to that of the surrounding medium ($n_{\text{air}} \approx 1$) and the cross-section geometry of the structures, the light can be confined inside by internal reflections. The light beams travel the same optical path within the cavity, producing interference between successive beams. This interference pattern is reflected in the form of modulations in the photoluminescence spectrum, as observed in part c of the figure. In our case, the cross section of the structures is a rectangle which allows two types of resonant modes (Figure 9d), Fabry-Perot (FP) or Whispering Gallery (WG). However, the WG modes cannot be established since some of the angles are well below the critical angle for internal reflection, approximately 30° . For FP cavities, the length of the optical path (δ_{op}) can be calculated as

$$\Delta\lambda = \frac{\lambda^2}{\delta_{\text{op}}n} \quad (1)$$

where n is the material refractive index, λ is the wavelength and $\Delta\lambda$ is the separation between resonant modes. In our case, this calculation gives an optical path length of 25.9 μm which agrees well with the lateral dimension of the structure, confirming that FP modes are formed.

The cavity can be further characterized calculating the quality factor (Q) and finesse (F) by

$$Q = \frac{\lambda_{\text{max}}}{\Gamma} \quad F = \frac{\Delta\lambda}{\Gamma} \quad (2)$$

where Γ is the FWHM for each λ . The obtained values are shown in Table 1 and are similar to those reported by other authors^[31] indicating the good quality of the cavity.

Table 1. Calculated quality (Q) factor and finesse (F) for each wavelength.

λ [nm]	Q	F
490.36	77.77	0.78
495.78	50.45	0.55
501.48	58.14	0.66
507.35	76.43	0.88
513.45	72.43	0.86
519.23	72.97	0.81
525.8	87.93	1.10
532.82	82.71	1.09
539.8	79	1.02
547.32	69.26	0.95
554.49	48.36	0.62
562.57	52.97	0.78
570.08	57.23	0.85
578.97	51.32	0.79
587.39	62.35	0.89
596.4	46.01	0.69
605.57	51.71	0.78

3. Conclusions

Nano- and micro- elongated structures of Tb–Li codoped ZnO have been grown by a vapor–solid method. A diversity of morphologies is obtained, varying between ribbons, wires and sword-like structures depending on the initial Li₂O amount used, and on the furnace zone where they growth which is directly related to the growth temperature. Besides, the size, face regularity and number of structures also depends on the quantity of Li₂O added, with better results achieved for the higher value. The amount of Tb incorporated depends on the morphology of the structures and varies between 3 and 13 at%, this variation seems to be related to the different Li incorporation which leads to distinct morphologies. Both XRD and Raman show the good crystalline quality of the structures which show ZnO wurtzite structure. As no shifts in any of the XRD maxima or Raman modes are observed, Tb incorporation as Tb⁴⁺ ions are more likely to occur, although a small quantity of Tb³⁺ ions seem to be also present as luminescence spectra suggest. Li also affects the luminescent emission of the structures. Its possibility to occupy either interstitial or substitutional positions modifies the defect structure and concentration of ZnO which is reflected in the intensity and shape of the luminescence bands. Finally, μ -PL experiments show that the structures can act as optical waveguides and resonant cavities, where Fabry–Perot modes are formed.

4. Experimental Section

The samples were prepared from a mixture of ZnS, Tb₄O₇, and Li₂O powders (99.999, 99.9, and 99.5% purity, respectively). In all cases, the Tb₄O₇ weight content was fixed at 5% (1.3 at% when only Tb is present) while the Li₂O weight content was selected at 1%, 5%, and 10% (3, 13, and 23 at%, respectively). The mixtures were homogenized by ball milling in a centrifugal ball mill with 20 mm agate balls for 5 h. The final powder was compacted under a compressive load to form disk shaped samples of about 7 mm diameter and 2 mm thickness. To obtain the structures, the samples were then placed on an alumina boat and annealed in a horizontal furnace with a quartz tube at 950 °C during 10 h under constant gas flow. The growth set-up has been described elsewhere.^[32] In the present work, 1.0 L min^{−1} of N₂ has been used.

Secondary electron images were recorded either in a Leica 440 SEM or FEI Inspect SEM. CL spectra were carried out in a Hitachi S2500 SEM at room temperature with a beam energy between 15 and 20 keV using a HAMAMATSU PMA-11 charge coupled device camera. EDS was performed with a Bruker AXS Quantax system in a Leica 440 SEM. XRD measurements were performed in a Philips diffractometer using Cu K α radiation. Micro-photoluminescence (μ -PL) and Raman experiments were performed at room temperature in a Horiba JovinYvon LabRAM HR800 confocal microscope with a He–Cd ($\lambda_{\text{ex}} = 325$ nm) or He–Ne ($\lambda_{\text{ex}} = 632.8$ nm) laser as excitation source, respectively. For μ -PL, a custom designed module allows to separate excitation and collection point.^[33]

Acknowledgements

This work was founded by the Complutense University of Madrid- Banco Santander via project UCM-Santander 2019 (PR87/19-22613) and Complutense University—Comunidad de Madrid via project PR65/19-22464 and the Spanish Ministry of Science, Innovation and Universities via project MINECO/FEDER-MAT2015-65274-R.

Conflict of Interest

The authors declare no conflict of interest.

Data Availability Statement

The data that support the findings of this study are available from the corresponding author upon reasonable request.

Keywords

luminescence, optical cavities, rare earth doping, ZnO

Received: December 2, 2021

Revised: January 18, 2022

Published online: February 19, 2022

- [1] Z. L. Wang, *J. Phys. Condens. Matter* **2004**, *16*, R829.
- [2] P. Singh, R. Kumar, R. K. Singh, *Ind. Eng. Chem. Res.* **2019**, *58*, 17130.
- [3] V. Kumar, O. M. Ntwaeaborwa, T. Soga, V. Dutta, H. C. Swart, *ACS Photonics* **2017**, *4*, 2613.
- [4] C. Shan, M. Zhao, D. Jiang, Q. Li, M. Li, X. Zhou, Y. Duan, N. Wang, R. Deng, *Nanotechnology* **2019**, *30*, 305703.
- [5] D. Vanmaekelbergh, L. K. Van Vugt, *Nanoscale* **2011**, *3*, 2783.
- [6] J. Theerthagiri, S. Salla, R. A. Senthil, P. Nithyadharani, A. Madankumar, P. Arunachalam, T. Maiyalagan, H. S. Kim, *Nanotechnology* **2019**, *30*, 392001.
- [7] K. M. Lee, C. W. Lai, K. S. Ngai, J. C. Juan, *Water Res.* **2016**, *88*, 428.
- [8] K. Qi, B. Cheng, J. Yu, W. Ho, *J. Alloys Compd.* **2017**, *727*, 792.
- [9] J. L. Frieiro, C. Guillaume, J. López-Vidrier, O. Blázquez, S. González-Torres, C. Labbé, S. Hernández, X. Portier, B. Garrido, *Nanotechnology* **2020**, *31*, 465207.
- [10] E. Cerrato, C. Gionco, I. Berruti, F. Sordello, P. Calza, M. C. Paganini, *J. Solid State Chem.* **2018**, *264*, 42.
- [11] A. Urbieto, R. del Campo, R. Pérez, P. Fernández, J. Piqueras, *J. Alloys Compd.* **2014**, *610*, 416.
- [12] R. Khanum, N. M. Das, R. S. Moirangthem, *J. Appl. Phys.* **2019**, *125*, 173107.
- [13] R. Ariza, B. Sotillo, F. Pavon, A. Urbieto, P. Fernández, *Appl. Sci.* **2020**, *10*, 8602.
- [14] F. Pavón, A. Urbieto, P. Fernández, *J. Lumin.* **2018**, *195*, 396.
- [15] P. Kumar, A. K. Yadav, A. G. Joshi, D. Bhattacharyya, S. N. Jha, P. C. Pandey, *Mater. Charact.* **2018**, *142*, 593.
- [16] P. P. Pal, J. Manam, *Nanosystems* **2013**, *4*, 395.
- [17] C. H. Park, S. B. Zhang, S. H. Wei, *Phys. Rev. B Condens. Matter Mater. Phys.* **2002**, *66*, 1.
- [18] A. K. Singh, S. K. Singh, S. B. Rai, *RSC Adv.* **2014**, *4*, 27039.
- [19] R. Ariza, F. Pavón, A. Urbieto, P. Fernández, *J. Phys. Chem. Solids* **2020**, *139*, 109354.
- [20] R. Cuscó, E. Alarcón-Lladó, J. Ibáñez, L. Artús, J. Jiménez, B. Wang, M. J. Callahan, *Phys. Rev. B Condens. Matter Mater. Phys.* **2007**, *75*, 1.
- [21] T. C. Damen, S. P. S. Porto, B. Tell, *Phys. Rev.* **1966**, *142*, 570.
- [22] T. Tatsumi, M. Fujita, N. Kawamoto, M. Sasajima, Y. Horikoshi, *J. Appl. Phys. Part 1* **2004**, *43*, 2602.
- [23] K. Vanheusden, C. H. Seager, W. L. Warren, D. R. Tallant, J. A. Voigt, *Appl. Phys. Lett.* **1995**, *68*, 403.
- [24] R. A. Rakesh, S. Balakumar, *Process. Appl. Ceram.* **2014**, *8*, 7.
- [25] N. Shakti, C. Devi, A. K. Patra, P. S. Gupta, S. Kumar, *AIP Adv.* **2018**, *8*, 1.

- [26] Y. W. Heo, D. P. Norton, S. J. Pearton, *J. Appl. Phys.* **2005**, *98*, 073502.
- [27] X. M. Teng, H. T. Fan, S. S. Pan, C. Ye, G. H. Li, *J. Appl. Phys.* **2006**, *100*, 053507.
- [28] G. Li, X. Lu, C. Su, Y. Tong, *J. Phys. Chem. C* **2008**, *112*, 2927.
- [29] J. Liu, S. Lee, Y. H. Ahn, J.-Y. Park, K. H. Koh, K. H. Park, *Appl. Phys. Lett.* **2008**, *92*, 263102.
- [30] X. Zhang, X. Zhang, J. Xu, X. Shan, J. Xu, D. Yu, *Opt. Lett.* **2009**, *34*, 2533.
- [31] V. V. Ursaki, A. Burlacu, E. V. Rusu, V. Postolake, I. M. Tiginyanu, *J. Opt. A Pure Appl. Opt.* **2009**, *11*, 075001.
- [32] R. Ariza, M. Dael, B. Sotillo, A. Urbieto, J. Solis, P. Fernández, *J. Alloys Compd.* **2021**, *877*, 160219.
- [33] R. M. Ma, X. L. Wei, L. Dai, S. F. Liu, T. Chen, S. Yue, Z. Li, Q. Chen, G. G. Qin, *Nano Lett.* **2009**, *9*, 2697.